

The origin of low bandgap and ferroelectricity of a co-doped BaTiO₃

Phuyal, D.; Das, S.; Mukherjee, S.; Jana, S.; Kvashnina, K. O.; Sarma, D. D.; Karis, O.; Rensmo, H.; Butorin, S. M.;

Originally published:

November 2018

EPL - Europhysics Letters 124(2018), 27005

DOI: <https://doi.org/10.1209/0295-5075/124/27005>

Perma-Link to Publication Repository of HZDR:

<https://www.hzdr.de/publications/Publ-27701>

Release of the secondary publication
on the basis of the German Copyright Law § 38 Section 4.

The origin of low bandgap and ferroelectricity of a co-doped ferroelectric

Dibya Phuyal¹, Shyamashis Das², Soham Mukherjee¹, Somnath Jana¹, Kristina O. Kvashnina^{3,4}, D.D. Sarma², Olof Karis¹, Håkan Rensmo¹, Sergei M. Butorin¹

¹ Division of Molecular & Condensed Matter Physics, Department of Physics and Astronomy, Uppsala University, Box 516, SE-75121, Uppsala, Sweden

² Department of Solid State and Structural Chemistry Unit, Indian Institute of Science, Bengaluru 560012, India

³ Rossendorf Beamline at ESRF – The European Synchrotron, CS40220, 38043 Grenoble Cedex 9, France

⁴ Helmholtz Zentrum Dresden-Rossendorf (HZDR), Institute of Resource Ecology, PO Box 510119, 01314 Dresden, Germany

Email: dibya.phuyal@physics.uu.se

We recently demonstrated a new low bandgap ferroelectric material based on BaTiO₃. The co-doping of BaTiO₃ exhibited robust spontaneous electrical polarization with bandgap values suitable for visible light absorption for application in optoelectronic devices. In this study, the valence and conduction bands are investigated with a combination of x-ray spectroscopies and DFT calculations. The local electronic structure and coordination of BaTi_{1-x}(Mn_{1/2}Nb_{1/2})_xO₃ is studied by means of x-ray absorption at the Ti *K*, Mn *K*, and O *K* edges. The spectroscopic evidence suggests only small distortions to the parent tetragonal ferroelectric system, reducing of the bandgap through compositional doping without compromising ferroelectricity to a large extent. The Ti *K* pre-edge features in particular, which are sensitive to site coordination and an indication of Ti off-centering within the Ti-O₆ octahedra, shows modest changes with doping and strongly corroborates with our measured polarization values. Resonant photoemission spectroscopy results reveal newly created Mn *d* bands that hybridize with O *2p* as well as additional valence band edge states with predominantly Mn *d* character. Through various x-ray spectroscopic techniques, we reveal the electronic structure that allows the compound to retain its ferroelectricity while reducing the bandgap.

BaTiO₃ is a prototypical ferroelectric oxide and is of a special interest for its room temperature polarization and used in many applications^{1,2}. Ferroelectrics have a spontaneous polarization and can be switched with an external stimulus. They have been shown to produce a bulk photovoltaic effect (BPVE)³⁻⁵, in which charge carriers in the bulk are separated by the inherent polarization, countering charge recombination⁶. Very recently, Spanier *et. al.* and colleagues showed how BaTiO₃ (BTO) in a photovoltaic architecture may break the Shockley-Queisser limit yielding greater-than-unity quantum efficiency and an above band-gap photovoltage of 8.2 eV⁷. This remarkable result demonstrates the tremendous potential for ferroelectric absorbers in photovoltaics and other light-harvesting applications. However, bulk BaTiO₃ is only able to harvest a tenth of the solar spectrum, limited primarily by the large bandgap (3.2 eV) in the charge-transfer insulator.

We recently reported a series of barium titanates (BaTiO₃) co-doped with transition metal (TM) ions, namely Jahn-Teller distorted Mn³⁺ and a *d*⁰ Nb⁵⁺ ions⁸. This new class of oxides exhibits ferroelectricity with tunable bandgaps in the range of 1.5 – 3.2 eV, suitable for visible light absorption. The partial replacement of Ti⁴⁺ with finite *d* electrons (*d*^{*n*}) from transition metal ions (Mn³⁺) maintains the tetragonal symmetry distortion while reducing the optical charge-transfer gap. The doping with a charge compensating *d*⁰ (Nb⁵⁺) - with its similar *d*⁰ configuration to Ti - should provide the necessary polarization at the B-site⁹. The BaTi_{1-x}(Mn_{1/2}Nb_{1/2})_xO₃ (hereafter referred as BTMNO) remnant polarization (*P_r*) was retained to a large extent, as much as 70% of BaTiO₃ for the *x* = 0.075 sample (*E_g* = 1.66 eV). Therefore, the changes in the crystal and electronic structure at the B site can offer insights to how ferroelectricity

persists while modifying the bandgap. Overall, the site-specific substitution with Mn and Nb ions presents an effective strategy in retaining much of the instantaneous polarization with bandgap tuning.

In this letter, we report on the electronic structure properties of BTMNO using a combination of x-ray spectroscopies and DFT calculations and systematically follow changes in the electronic structure as a function of doping. In addition to assigning the formal valences of the *B*-site ions, we have used resonant photoemission spectroscopy (ResPES) to establish doping induced growth of new states with predominant Mn *d* character. Together, absorption and photoemission results elucidate the covalence of *B*-site bonding with oxygen that is the prevalent characteristic of BaTiO₃ based ferroelectrics. We have used this approach to characterize both bulk polycrystalline pellets and epitaxial thin films. Our experimental results are in good agreement with DFT calculations.

Polycrystalline BaTiO₃ and the Mn_{1/2}/Nb_{1/2} doped pellets were synthesized using conventional solid-state procedure described in our previous work⁸. All compositions up to *x* = 0.075 showed tetragonal symmetry, while *x* = 0.10 is cubic. BTO and doped BTMNO thin films were epitaxially grown on a conducting niobium-doped single-crystal STO (100) by Pulsed Laser Deposition (PLD) with targets ablated at 750 mJ cm⁻² for BTO and 1 J cm⁻² for BTMNO. The oxygen partial pressure was kept at 0.055 mBar and 650° C for BTO and 700° C for BTMNO and annealed for 1 hour in atmospheric pressure followed by cooling to room temperature at 5° C/min. High-resolution XRD was used to establish epitaxial growth and

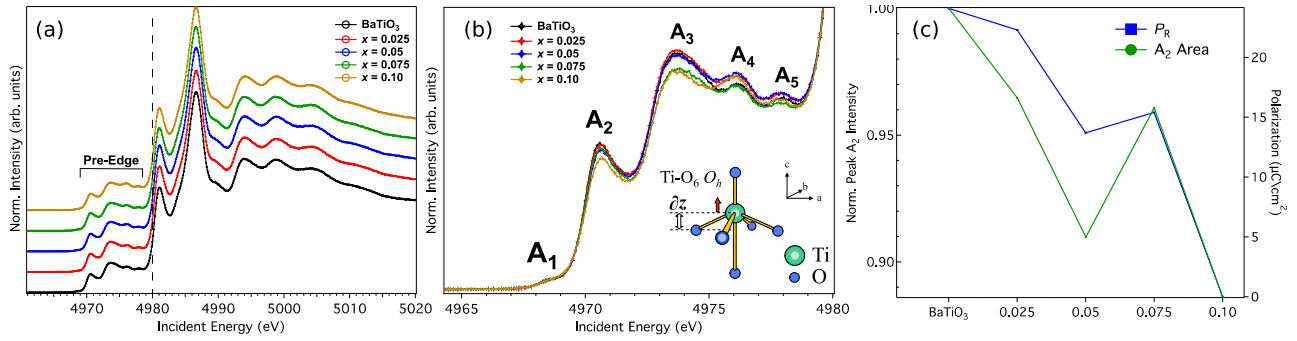


FIG. 1. (a) Ti K Edge HERFD-XANES for the BTMNO series where the main absorption energy position (E_0) is indicated with a vertical dashed line. The spectral profiles are nearly identical, showing only modest changes to the local Ti displacive-type ferroelectricity and broken inversion symmetry is maintained. The spectra are normalized to the edge-jump and shifted vertically for presentation. (b) Magnified pre-edge features for the BTMNO series. The modest change in the intensities of the quadrupolar transitions ($1s \rightarrow 3d$, peaks A_1 and A_2) states indicate that the Ti off-centering is maintained. (c) The polarization behavior in the series is consistent with measured A_2 peak intensity.

tetragonal phase purity. X-ray reflectivity (XRR) was used to determine the film thickness.

High Energy Resolution Fluorescence Detected X-ray Absorption Near Edge Structure (HERFD-XANES, henceforth referred to HERFD) experiments were performed at the ID26 beamline at the European Synchrotron Radiation Facility^{10–13}. Ti K and Mn K absorption spectra were collected set to the $K\beta_{1,3}$ emission line ($3p \rightarrow 1s$) using Ge (331) and Ge (444) crystal analyzers respectively. The analyzer crystals were arranged with the sample and detector (avalanche photodiode) in a vertical Rowland geometry ($R \approx 1$ m). The overall resolution of HERFD data is determined by the full width at half maximum of the elastic profile, which was about 0.5 eV. O K XAS spectra was taken at the soft x-ray beamline at 8.0.1 at the Advanced Light Source (Berkeley, CA) and acquired in total fluorescence yield mode (TFY) and under vacuum (10^{-8} mBar). Soft x-ray photoelectron spectroscopy was carried out at the I09 beamline at the Diamond Light Source (UK). The resonant photon energy was selected at the maximum of the x-ray absorption (XAS) peak measured in total electron yield (TEY) mode. Photoelectron spectra were recorded using a VG Scienta EW4000 high-energy analyzer with a 30° acceptance angle. The resolution is approximately 330–400 meV. The base pressure of the main chamber was maintained at 10^{-10} mbar.

Figure 1(a) shows the Ti K HERFD-XANES spectra of the parent BaTiO_3 and $(\text{Mn}_{1/2}\text{Nb}_{1/2})$ co-doped BaTiO_3 compounds. Key attributes in HERFD-XANES data are the well-resolved pre-edge features that are otherwise smeared out due to the core-hole lifetime broadening in conventional fluorescence yield mode. The main absorption edge position (E_0) for the doped and undoped BaTiO_3 samples are approximately at the same energy position (~ 4980 eV, vertical dashed line in Fig. 1(a)), which show that the Ti ions for all samples are in the same oxidation state: Ti^{4+} . The most intense structures near ~ 4981 eV and ~ 4986 eV are due to transitions from Ti $1s \rightarrow 4p$ states. The higher energy side of the spectrum ($E_{in} > 5000$ eV)

consists of multiple-scattering contribution within the TiO_6 octahedra. The spectral features far into the continuum for doped and undoped samples are almost unchanged in their profile.

HERFD-XANES spectra allow for a more precise separation of weak pre-edge structures compared to conventional x-ray absorption spectroscopy, particularly for dilute systems. The intensities and relative energies of metal K pre-edge features have high sensitivity to both local geometry and electronic structure. The pre-edge structures are characteristic of dipolar and quadrupolar transitions, *i.e.* from Ti $1s \rightarrow 3d$ quadrupole and Ti $1s \rightarrow 4p$ dipolar transitions. Figure 1(b) shows the evolution of the pre-edge peaks as a function of doping. In non-centrosymmetric crystal structures, the presence of pre-edge peaks is enhanced in contrast to structures with inversion symmetry^{14–16}. The first two peaks in the pre-edge set (peak labeled A_1 & A_2) directly relate to the quadrupolar $1s$ - $3d$ t_{2g} and into mixed Ti $e_g - \text{O } 2p$ transitions respectively^{14,17,18}. Features A_3 , A_4 , and A_5 have large contributions from Ti p -states and oxygen states. The intensity of peaks A_2 - A_5 decrease progressively upon increased doping with Mn/Nb ions when compared with BaTiO_3 . The extent of off-centering of Ti atom can be directly related to the relative change in intensity of the pre-edge A_2 peak^{19,20}. The magnitude of displacement, defined by fitting the area under peak A_2 with a Gaussian and arctangent background, is particularly high for the $x = 0.025$ and $x = 0.05$ doped samples, where Mn and Nb d orbitals also mix with O $2p$ states. Figure 1(c) shows the remnant polarization (P_R) and peak A_2 area as a function of increased doping – following the same trend. The increase in P_R for the $x = 0.075$ sample compared to $x = 0.05$ is also revealed in the peak area from the Ti K pre-edge spectra. This finding indicates that the Ti atom is still off-centered with respect to the octahedral cage of surrounding oxygen atoms, thereby retaining ferroelectricity through doping of $3d$ (Mn) and $4d$ (Nb) transition metals.

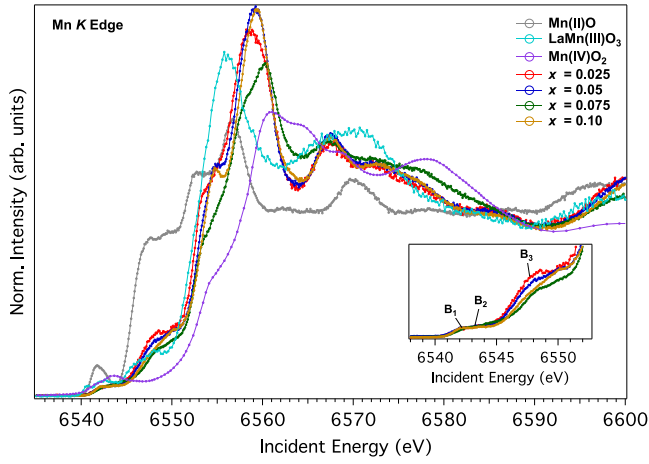


FIG. 2. Normalized Mn *K* HERFD-XAS measured at room temperature using the $K\beta_{1,3}$ emission line. The inset shows the pre-edge region with the quadrupolar (B_1 and B_2) and dipolar peaks.

The HERFD-XANES spectra across the Mn *K* edge is shown in Figure 2. The spectra is compared against MnO (II), a perovskite LaMnO_3 ²¹ (III), and MnO_2 (IV) as references to identify the formal oxidation state. As noted in related Mn *K* HERFD studies^{22,23}, the energy position of the main edge is correlated with the formal valence state of the Mn atom. The main absorption edge clearly appears at a higher energy (by several eV) for the BTMNO samples in contrast to the Mn^{2+} MnO and below the Mn^{4+} MnO_2 references. The sharp main line are transitions to Mn $4p$ bands. The main line exhibits a slight change for the 7.5% doped sample, which could imply competing distortions from off-centering and first order Jahn-Teller distortion. The pre-edge structure also shows a change in intensity as a function of doping as shown in the inset of Figure 2. The two resolved peaks, labeled B_1 and B_2 are tentatively accounted as quadrupole Mn $1s \rightarrow 3d$ transitions, although is the subject of varying interpretations and debate in literature^{24,25}. While the B_1 and B_2 peak structures seem to be invariant in intensity and energy position regardless of the doping concentration, the B_3 peak is noticeably different. This structure has been argued as transition to the $3d$ states of neighboring metal sites through the oxygen mediated inter-site hybridization of $\text{TM}(4p)\text{-O}(2p)\text{-TM}'(3d)$ and correspondingly occur at higher energies^{18,22,26}. Peak B_3 is attenuated monotonically in intensity as a function of doping, with the exception of $x = 0.075$. This structure could be related to the Mn-O bond length and Mn-O-Mn bond angle for the $x = 0.075$ sample, as it also relates to the anomaly of the $x = 0.075$ remnant polarization, which requires a more detailed study.

The oxygen *K* edge can provide complementary information on the role of dopants in the bonding of the doped compounds as shown in Figure 3. In the case of transition metal oxides, the O $1s$ core-hole during the XAS process is expected to weakly interact with valence electrons of the TM ions, thus these measurements are expected to provide an unperturbed probe of unoccupied electronic states^{27,28}. The many structures correspond to excitations from oxygen $1s$ orbital to O p states hybridized with doped TMs and Ti/Ba states as labeled in Figure 3^{29,30}. The first two features undergo a change in both

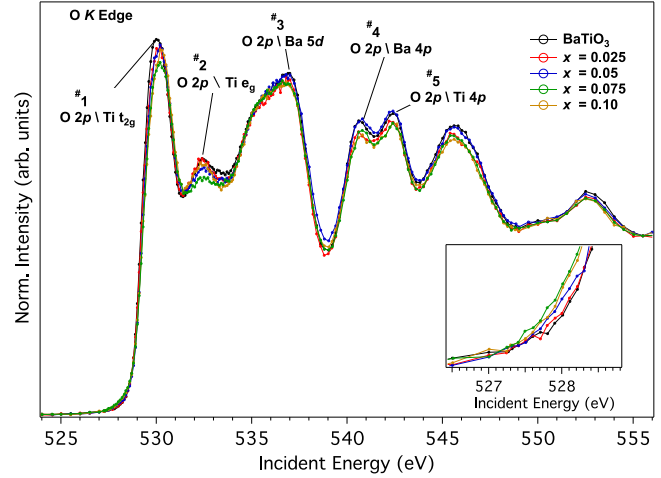


FIG. 3. O *K* edge of the series with pre-edge O *K* showing newly hybridized states with Mn and Nb d states. The LDA+U calculations also predict the hybridized O $2p$ /TM d states at the onset of the conduction band, where the top of the occupied oxygen $2p$ states is set to zero in the energy scale.

shape and peak energy as doping is increased. The third and fourth features are O $2p$ states hybridized with Ba $5d$ and $4p$ states respectively, which are formally identical in all samples. The main distinguishing feature between the doped and undoped samples is the increase in spectral weight at the onset of the main absorption line (~ 528 eV) as doping increases (inset of Figure 3). This indicates that the material new unoccupied states at the vicinity of the CB, which shift in the presence of dopants.

To evaluate the dopant effects on band edge states from experimental absorption and photoemission spectra, LDA+U DFT calculations using a projector augmented wave (PAW) method implement with the Generalized Gradient Approximation (GGA) potential was carried out in VASP^{31,32}

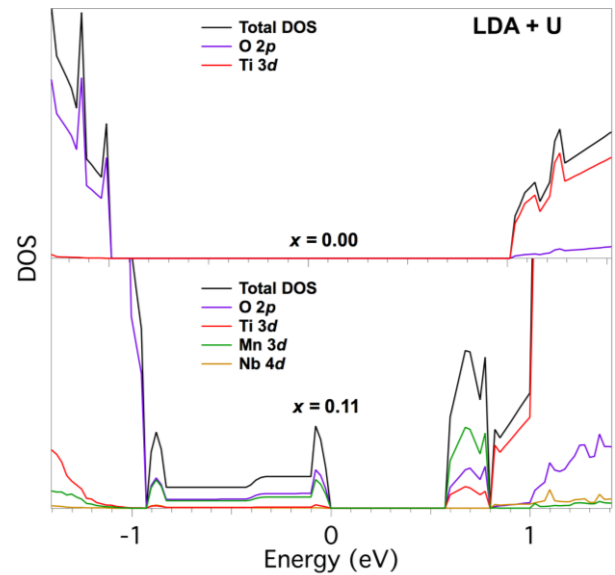


FIG. 4. Total and partial orbital-projected density of states for BaTiO_3 (top) and $x = 0.11$ (bottom) composition. The TM dopants introduce new bands at the edges of both valence and conduction bands respectively.

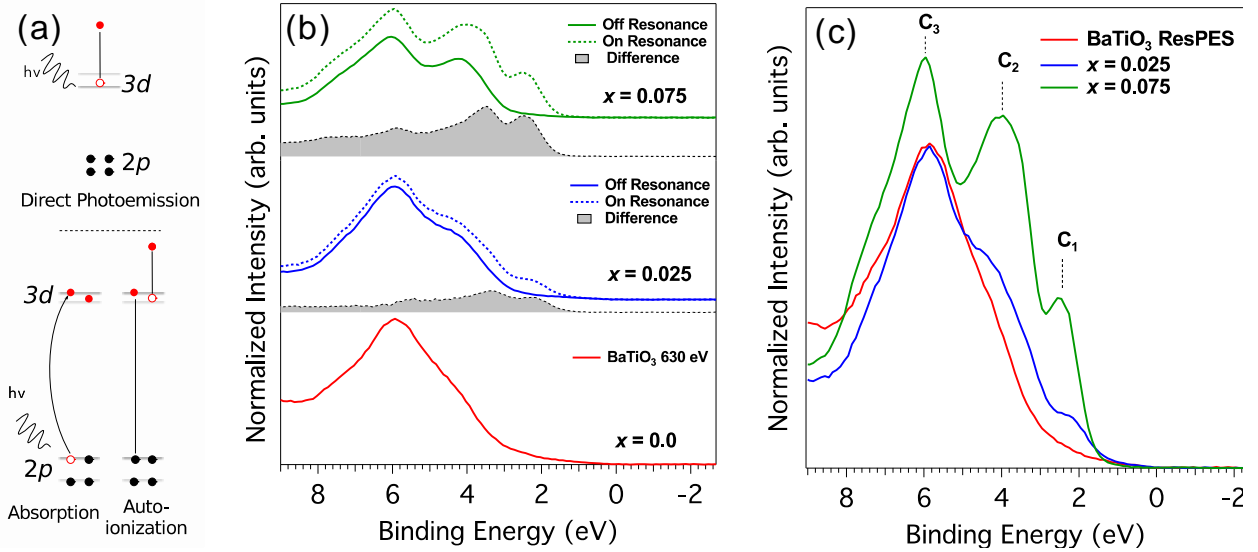


FIG 5. (a) A schematic representation of the excitation channels involved in the resonant photoemission process. (b) Resonant photoemission spectra for doped and undoped samples in the off-resonance ($h\nu = 630$ eV) and on-resonance condition ($h\nu = 640.2$ eV). The shaded area represents the difference between the on and off-resonance condition. The photoemission spectra are normalized to the Ba $5p$ peak (~ 15 eV). (c) The three resonating features for the $x = 0.025$ and $x = 0.075$ are assigned to Mn d states.

and shown in Figure 4. GGA+U calculation was performed with a U value of 4 eV on the dopant Mn $3d$ states and consistent with earlier doped BTO compositions³³. Electronic density of states is computed from the geometry optimized structure to get a qualitative understanding of the effect of doping on the band edges for $x \sim 11.1\%$ Mn and Nb co-doped BaTiO₃ composition. As usual, the bandgaps are underestimated in standard DFT calculations. The presence of dopant states at the onset of the conduction band result in the formation split-off O $2p$ states that are hybridized with primarily Mn d character, in agreement with the O K edge absorption spectra.

Due to the small Mn and Nb concentrations in the samples, the cross-sections for x-ray emission are exceedingly weak to demonstrate any meaningful information regarding the occupied Mn valence states. Furthermore, polycrystalline pellets are prone to charging during photoemission experiments. Therefore, BTO and co-doped thin films were fabricated in order to determine the changes to the valence band states by resonant photoemission spectroscopy (ResPES). From the results of DFT calculations (see Fig 4), the presence of new states at the band edge with predominant Mn $3d$ character is primarily responsible for decreasing the overall bandgap of this material. The resonant photoemission process enhances the spectral weight in the density of states in the valence band. In this condition, for a $3d$ transition metal the direct photoemission channel ($3d^n \rightarrow 3d^{n-1} + e^-$) can interfere with the autoionization channel triggered by the creation of a core hole ($2p^5 3d^{n+1} \rightarrow 2p^6 3d^{n-1} + e^-$). A schematic of the absorption and decay process is shown in Figure 5(a). The resonant condition is met by the photoabsorbed electron interfering with the auger emission, as shown on the lower panel of the schematic. In the absorption $2p$ - $3d$ process, which is followed by the autoionization process, the transition is denoted as resonant auger as opposed to normal auger emission.

Figure 5(b) shows the ResPES on thin films collected at the maximum of Mn $L_{2,3}$ absorption edge. The data is presented alongside with photon energy below the absorption threshold (630 eV), which results in a normal autoionization process rather than a resonant photoemission process. In the on-resonance case, the presence of additional electronic states are detected with photons at the Mn L resonance conditions only (~ 640.2 eV). As shown by the resonant enhancement at the Mn L edge, electronic states near E_F receive a dominant contribution from Mn $3d$ states. Three resonating behavior originating from the Mn $3d$ components are observed at 6, 4, and 2 eV B.E (marked by C_1 , C_2 , C_3 in Fig. 5(c)). Feature C_2 and C_3 (~ 4 and 6 eV B.E.) are in the region occupied primarily by O $2p$ states. Therefore we can argue that Mn $3d$ states have significant hybridization with O $2p$ states in the valence band and is predominantly responsible for reducing the bandgap of the doped compounds. The on-off resonance difference spectra, denoted by the gray shaded area (Fig. 5b), provides a direct probe for selective separation of the uppermost Mn $3d$ states. For both doped samples, although the spectral shapes are similar, the intensities are quite different as peaks C_1 , C_2 , and C_3 all show a larger enhancement when compared with $x = 0.025$ film. Our DFT calculations show that the Jahn-Teller Mn³⁺ ions control the splitting of the midgap states, which we associate with peaks C_2 and C_3 . The valence band maximum (VBM) is also shifted for both the doped samples, showing the effective narrowing of the bandgap with increasing doping content compared to the parent BaTiO₃.

In summary, the electronic structure of low band gap BaTi_{1-x}(Mn_{1/2}Nb_{1/2})_xO₃ ferroelectric was studied by means of a combined x-ray spectroscopy and DFT calculations. A detailed study on the electronic structure was performed to provide spectroscopic evidence of the reported ferroelectricity and reduced band gap functionality in these co-doped ferroelectrics based on BaTiO₃. The HERFD-XANES data showed that the off-centering of Ti ion persists relative to BaTiO₃ even at higher doping concentrations, although the extent is lowered.

The Mn ions assume a formal valence of 3+ regardless of the doping concentration. The overall changes to the valence band was verified by ResPES with the enhancement of additional Mn 3d states towards the Fermi level, and significant hybridization with O 2p that allows the band gap to reduce without compromising ferroelectricity to a large extent. These extra states created due to doping has predominantly Mn d character as shows from our DFT calculations, thereby establishing the role of Mn³⁺ ions in reducing the bandgap in BTMNO systems. This work shows the efficacy of x-ray based spectroscopy to investigate Ti off-centering as well as valence band properties.

Acknowledgements

We thank Diamond Synchrotron, ESRF, and ALS for their allocation of beamtime. We also thank Marcin Sikora for providing the reference spectrum for LaMnO₃. This work was supported by Swedish Government through “STandUP for ENERGY”, The Swedish Energy Agency, The Swedish Research Council, and the Knut & Alice Wallenberg Foundation. The calculations presented here made use of Thematic Unit of Excellence Facility at IISc Bengaluru.

References

- ¹ J.F. Scott, *Science* **315**, 954 (2007).
- ² M. Dawber, K.M. Rabe, and J.F. Scott, *Rev. Mod. Phys.* **77**, 1083 (2005).
- ³ V.M. Fridkin, *Crystallogr. Reports* **46**, 654 (2001).
- ⁴ A. Zenkevich, Y. Matveyev, K. Maksimova, R. Gaynutdinov, A. Tolstikhina, and V. Fridkin, *Phys. Rev. B - Condens. Matter Mater. Phys.* **90**, 1 (2014).
- ⁵ S.M. Young and A.M. Rappe, *Phys. Rev. Lett.* **109**, 116601 (2012).
- ⁶ P. Lopez-Varo, L. Bertoluzzi, J. Bisquert, M. Alexe, M. Coll, J. Huang, J.A. Jimenez-Tejada, T. Kirchartz, R. Nechache, F. Rosei, and Y. Yuan, *ACS Energy Lett.* **3**, 1176 (2018).
- ⁷ J.E. Spanier, V.M. Fridkin, A.M. Rappe, A.R. Akbashev, A. Polemi, Y. Qi, Z. Gu, S.M. Young, C.J. Hawley, D. Imbrenda, G. Xiao, A.L. Bennett-Jackson, and C.L. Johnson, *Nat. Photonics* **10**, 611 (2016).
- ⁸ S. Das, S. Ghara, P. Mahadevan, A. Sundaresan, J. Gopalakrishnan, and D.D. Sarma, *ACS Energy Lett.* **3**, 1176 (2018).
- ⁹ N. Hill, *J. Phys. Chem. B* **104**, 6694 (2000).
- ¹⁰ C. Gauthier, V.A. Solé, R. Signorato, J. Goulon, and E. Moquiline, *J. Synchrotron Radiat.* **6**, 164 (1999).
- ¹¹ A.J. Atkins, C.R. Jacob, and M. Bauer, *Chem. - A Eur. J.* **18**, 7021 (2012).
- ¹² M. Bauer, *Phys. Chem. Chem. Phys.* **16**, 13827 (2014).
- ¹³ P. Glatzel and U. Bergmann, *Coord. Chem. Rev.* **249**, 65 (2005).
- ¹⁴ R. V Vedrinskii, V.L. Kraizman, A.A. Novakovich, P. V Demekhin, and S. V Urazhdin, *J. Phys. Condens. Matter* **10**, 9561 (1998).
- ¹⁵ B. Ravel, E.A. Stern, R.I. Vedrinskii, and V. Kraizman, *Ferroelectrics* **206**, 407 (1998).
- ¹⁶ S. Matsuo, N. Sakaguchi, and H. Wakita, *Anal. Sci.* **21**, 805 (2005).
- ¹⁷ T. Yamamoto, T. Mizoguchi, and I. Tanaka, *Phys. Rev. B - Condens. Matter Mater. Phys.* **71**, 3 (2005).
- ¹⁸ F. De Groot, G. Vankó, and P. Glatzel, *J. Phys. Condens. Matter* **21**, 104207 (2009).
- ¹⁹ I. Levin, E. Cockayne, V. Krayzman, J.C. Woicik, S. Lee, and C.A. Randall, *Phys. Rev. B - Condens. Matter Mater. Phys.* **83**, 1 (2011).
- ²⁰ F.A. Rabuffetti and R.L. Brutchey, *ACS Nano* **7**, 11435 (2013).
- ²¹ M. Sikora, K. Knizek, C. Kapusta, and P. Glatzel, *J. Appl. Phys.* **103**, 1 (2008).
- ²² V. Cuartero, S. Lafuerza, M. Rovezzi, J. García, J. Blasco, G. Subías, and E. Jiménez, *Phys. Rev. B* **94**, 155117 (2016).
- ²³ S. Lafuerza, J. García, G. Subías, J. Blasco, and P. Glatzel, *Phys. Rev. B* **93**, 31 (2016).
- ²⁴ L. Hozoi, A.H. de Vries, and R. Broer, *Phys. Rev. B* **64**, 165104 (2001).
- ²⁵ J.M. Chen, C.K. Chen, T.L. Chou, I. Jarrige, H. Ishii, K.T. Lu, Y.Q. Cai, K.S. Liang, J.M. Lee, S.W. Huang, T.J. Yang, C.C. Shen, R.S. Liu, J.Y. Lin, H.T. Jeng, and C.C. Kao, *Appl. Phys. Lett.* **91**, 1 (2007).
- ²⁶ a Markowicz, D. Wegrzynek, E. Chinea-Cano, S. a Bamford, D.H. Torres, and R.P. Alvarez, *X-Ray Spectrom.* **36**, 27 (2007).
- ²⁷ F.M.F. De Groot, J. Faber, J.J.M. Michiels, M.T. Czyzyk, M. Abbate, and J.C. Fuggle, *Phys. Rev. B* **48**, 2074 (1993).
- ²⁸ E.Z. Kurmaev, R.G. Wilks, A. Moewes, L.D. Finkelstein, S.N. Shamin, and J. Kuneš, *Phys. Rev. B - Condens. Matter Mater. Phys.* **77**, 1 (2008).
- ²⁹ A. Chassé, S. Borek, K.-M. Schindler, M. Trautmann, M. Huth, F. Steudel, L. Makhova, J. Gräfe, and R. Denecke, *Phys. Rev. B* **84**, 195135 (2011).
- ³⁰ M. Bugnet, G. Radtke, and G.A. Botton, *Phys. Rev. B - Condens. Matter Mater. Phys.* **88**, 1 (2013).
- ³¹ G. Kresse and J. Furthmüller, *Phys. Rev. B - Condens. Matter Mater. Phys.* **54**, 11169 (1996).
- ³² G. Kresse and J. Furthmüller, *Comput. Mater. Sci.* **6**, 15 (1996).
- ³³ H.K. Chandra, K. Gupta, A.K. Nandy, and P. Mahadevan, *Phys. Rev. B - Condens. Matter Mater. Phys.* **87**, 1 (2013).